

# Stormy weather in 3C 196.1: nuclear outbursts and merger events shape the environment of the hybrid radio galaxy 3C 196.1

F. RICCI,<sup>1,2,3</sup> L. LOVISARI,<sup>1</sup> R. P. KRAFT,<sup>1</sup> F. MASSARO,<sup>4,5</sup> A. PAGGI,<sup>4</sup> E. LIUZZO,<sup>6</sup> G. TREMBLAY,<sup>1</sup> W. R. FORMAN,<sup>1</sup> S. BAUM,<sup>7,8</sup> C. O'DEA,<sup>7,9</sup> AND B. WILKES<sup>1</sup>

<sup>1</sup>Smithsonian Astrophysical Observatory, 60 Garden Street, Cambridge, MA 02138, USA

<sup>2</sup>Instituto de Astrofísica and Centro de Astroingeniería, Facultad de Física, Pontificia Universidad Católica de Chile, Casilla 306, Santiago 22, Chile

<sup>3</sup>Dipartimento di Matematica e Fisica, Università Roma Tre, via della Vasca Navale 84, 00146 Roma, Italy

<sup>4</sup>Dipartimento di Fisica, Università degli Studi di Torino, via Pietro Giuria 1, I-10125 Torino, Italy

<sup>5</sup>Consorzio Interuniversitario per la Fisica Spaziale (CIFS), via Pietro Giuria 1, I-10125, Torino, Italy

<sup>6</sup>Istituto di Radioastronomia, INAF, via Gobetti 101, 40129, Bologna, Italy

<sup>7</sup>University of Manitoba, Dept. of Physics and Astronomy, Winnipeg, MB R3T 2N2, Canada

<sup>8</sup>Center for Imaging Science, Rochester Institute of Technology, 84 Lomb Memorial Dr., Rochester, NY 14623, USA

<sup>9</sup>School of Physics & Astronomy, Rochester Institute of Technology, 84 Lomb Memorial Dr., Rochester, NY 14623, USA.

(Received Month day, 2018; Revised Month day, 2018; Accepted Month day, 2018)

Submitted to ApJ

## ABSTRACT

We present a multi-wavelength analysis based on archival radio, optical and X-ray data of the complex radio source 3C 196.1, whose host is the brightest cluster galaxy of a  $z = 0.198$  cluster. HST data show  $H\alpha$ + $[N\ II]$  emission aligned with the jet 8.4 GHz radio emission. An  $H\alpha$ + $[N\ II]$  filament coincides with the brightest X-ray emission, the northern hotspot. Analysis of the X-ray and radio images reveals cavities located at galactic- and cluster- scales. The galactic-scale cavity is almost devoid of 8.4 GHz radio emission and the south-western  $H\alpha$ + $[N\ II]$  emission is bounded (in projection) by this cavity. The outer cavity is co-spatial with the peak of 147 MHz radio emission, and hence we interpret this depression in X-ray surface brightness as being caused by a buoyantly rising bubble originating from an AGN outburst  $\sim 280$  Myrs ago. A *Chandra* snapshot observation allowed us to constrain the physical parameters of the cluster, which has a cool core with a low central temperature  $\sim 2.8$  keV, low central entropy index  $\sim 13$  keV cm<sup>2</sup> and a short cooling time of  $\sim 500$  Myr, which is  $< 0.05$  of the age of the Universe at this redshift. By fitting jumps in the X-ray density we found Mach numbers between 1.4 and 1.6, consistent with a shock origin. We also found compelling evidence of a past merger, indicated by a morphology reminiscent of gas sloshing in the X-ray residual image. Finally, we computed the pressures, enthalpies  $E_{cav}$  and jet powers  $P_{jet}$  associated with the cavities:  $E_{cav} \sim 7 \times 10^{58}$  erg,  $P_{jet} \sim 1.9 \times 10^{44}$  erg s<sup>-1</sup> for the inner cavity and  $E_{cav} \sim 3 \times 10^{60}$  erg,  $P_{jet} \sim 3.4 \times 10^{44}$  erg s<sup>-1</sup> for the outer cavity.

## 1. INTRODUCTION

Nuclear outflows from active galactic nuclei (AGN) have a dramatic impact on cosmic structure formation and evolution. These energetic outflows are invoked to explain the anti-hierarchical quenching of star formation in massive galaxies, the exponential cut-off at the bright end of the galaxy luminosity function, the black hole-host scaling relations and the quenching of cooling-flows in cluster cores (e.g. Scannapieco et al. 2005; Begelman & Nath 2005; Main et al. 2017). The mutual radio galaxy/cluster interaction is significant for both: the intra-cluster medium (ICM) can change

the jet propagation, while the great mechanical power of radio AGN can quench cooling in cluster cool cores.

One of the most important *Chandra* results in cluster science is the discovery of X-ray cavities and shocks (e.g. see reviews from McNamara & Nulsen 2007; Gitti et al. 2012), which are the smoking guns of the so-called radio- (or kinetic-, maintenance-) mode feedback (Bîrzan et al. 2008; Cavagnolo et al. 2010 for a review see Fabian 2012) of AGN, which are fed by the accretion of circumnuclear gas (e.g. Gaspari et al. 2015). The AGN energy released by the accretion process heats up or sweeps out the surrounding medium, reducing the accretion rate onto the black hole until it is switched off. When the gas cools down or it is replenished, e.g. through a merger with another galaxy, accretion can start

again. The new episode of accretion can eventually trigger the radio jets, closing the feedback loop.

The radio-mode feedback has been observed in cool core clusters (MS0735.6+7421 [McNamara et al. 2009](#); A2052 [Blanton et al. 2011](#); A2597 [Tremblay et al. 2012](#); M87 [Forman et al. 2017](#)), in groups (e.g. NGC 5813 [Randall et al. 2015](#)) and in isolated ellipticals (e.g. NGC 4636 [Jones et al. 2002](#)) where the ICM is heated up by AGN jet-inflated plasma bubbles that buoyantly rise in the hot, X-ray emitting atmosphere ([Churazov et al. 2013](#); [Su et al. 2017](#), see also [Boehringer et al. 1993](#); [Churazov et al. 2000, 2001](#) for the first *ROSAT* measurements in Perseus and Virgo). As the bubbles rise, their energy is converted into motions of the X-ray emitting plasma which, eventually, is converted into thermal energy.

Our group has conducted over the last 8 years a *Chandra* snapshot survey (see [Massaro et al. 2010, 2012, 2013, 2015, 2018](#); [Stuardi et al. 2018](#)) aimed at characterizing the X-ray radiation from jets, hotspots, nuclei and cluster emission of the most powerful, and probably most studied, radio galaxies known, the Third Cambridge Revised catalog (3CR, [Bennett 1962](#); [Spinrad et al. 1985](#)).

Our *Chandra* snapshot program allowed us to select targets for detailed analysis. 3C 196.1 is very promising: it is a hybrid morphology (both FR I and FR II, [Fanaroff & Riley 1974](#)) radio galaxy embedded in a  $kT \sim 4$  keV galaxy cluster and has convincing morphological signatures of radio galaxy/cluster interaction ([Massaro et al. 2012](#)), with structures in the X-ray clearly related to ongoing and past outbursts of the radio galaxy.

3C 196.1 lies at  $z = 0.198$  within a cluster of galaxies CIZA J0815.4-0308 observed by *ROSAT* ([Kocevski et al. 2007](#)). 3C 196.1 has been classified in the optical as a low-excitation radio galaxy (LERG, [Buttiglione et al. 2010](#)), and is associated with the brightest cluster galaxy (BCG), an elliptical cD galaxy, the dominant galaxy of a group of 14 others that lie within about 350 kpc from its core ([Baum et al. 1988](#)). [Madrid et al. \(2006\)](#) show that its near-infrared image is elliptical, presenting an elongated structure NE to SW, in the same direction as the inner scale jet. The same morphology is seen in the optical ([Baum et al. 1988](#); [de Koff et al. 1996](#)). The optical color gradients of 3C 196.1 show periodic shells that could reflect merging and galactic cannibalism ([Zirbel 1996](#)). The host galaxy has optical isophotes whose centroids clearly shift to the SW at small radii ([de Koff et al. 1996](#)). This suggests that a merger has occurred several dynamical times ago. In fact, stellar tidal debris from a merger wash out over a few dynamical times, while shells in stellar surface brightness, which can manifest as isophote centroid offsets, can be long-lived remnants.

In this work we investigate the physical conditions of the 3C 196.1 environment in order to shed light on ongoing in-

teraction between the AGN and surrounding medium. We present a multi-wavelength study based on radio, optical and X-ray archival data of 3C 196.1, aimed at investigating the morphology and the nature of the multiphase emitting gas, unveil the impact of past AGN outbursts and dissect merger signatures. The paper is organized as follows: in Sect. 2 radio, optical and X-ray archival data are presented; Sect. 3 describes the X-ray analysis, with imaging presented in Sect. 3.1, spectral analysis carried out in Sect. 3.2 and surface brightness profiles extracted and fitted in Sect. 3.3; in Sect. 3.4 we adopted two edge-enhancement methods to localize small-amplitudes wriggles in the surface brightness; in Sect. 4 the results are presented and finally Sect. 5 is devoted to summary and conclusions. We assumed a flat cosmology with  $H_0 = 72$  km s<sup>-1</sup> Mpc<sup>-1</sup>,  $\Omega_M = 0.27$ , and  $\Omega_\Lambda = 0.73$  ([Dunkley et al. 2009](#)). This means that for 3C 196.1, the angular scale is 3.197 kpc arcsec<sup>-1</sup> and the luminosity distance is 946 Mpc. For all the figures presented in this work, the standard astronomical orientation is adopted, i.e. north up and east to the left.

## 2. DATA

### 2.1. Radio data

We used high frequency 8.4 GHz Very Large Array (VLA) archival data to investigate the core region of the galaxy, whereas we used low frequency 147 MHz Giant Metrewave Radio Telescope (GMRT) archival data to study the diffuse emission in the cluster outskirts ( $\sim 500$  kpc, i.e.  $\sim 0.5 R_{500}^1$ ). These radio frequencies sample different spatial scales due to the angular resolution that each radio band can achieve. The high frequency 8.4 GHz VLA data shown in Fig. 1 (left panel, contours on top of the optical image) has been observed on 2 July 1995 with the VLA in configuration A, the restoring beam is ( $0'.3 \times 0'.3, 0^\circ$ ), the rms is  $9.13 \times 10^{-2}$  mJy/beam and the brightest peak is at  $\sim 1.37 \times 10^{-2}$  Jy/beam. The 8.4 GHz flux of the NE (SW) radio lobe is 71 (32) mJy.

The 147 MHz GMRT data has been retrieved from the TIFR GMRT Sky Survey Alternative Data Release (TGSSADR [Intema et al. 2017](#)) website<sup>2</sup>. The TGSS ADR ID number is R26D31 and is a mosaic image of 5 deg square. The 147 MHz emission contours are superposed on the X-ray emission in Fig. 2 (right panel, black contours). The restoring beam is ( $26'.96 \times 25'', 0^\circ$ ), the rms is 0.13 mJy/beam and the brightest peak is at  $\sim 16.9$  Jy/beam. The radio flux of the SW diffuse emission is 0.264 Jy at 147 MHz.

### 2.2. HST observation

<sup>1</sup>  $R_{500}$  defines the radius at which the over-density is equal to 500 times the critical density of the Universe at the cluster redshift.

<sup>2</sup> <http://tgssadr.strw.leidenuniv.nl/doku.php>

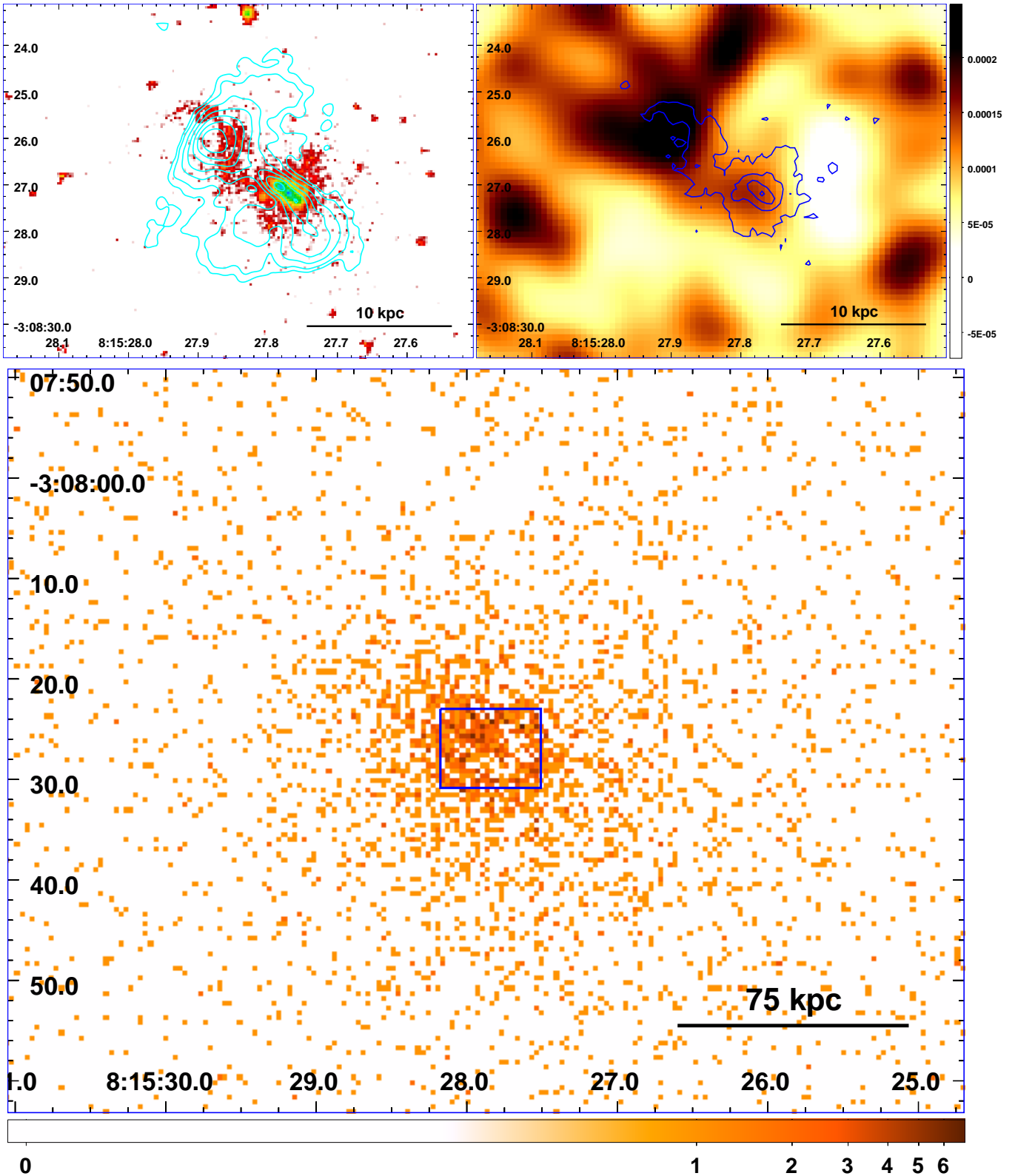


**Figure 1.** Images of the central BCG 3C 196.1 and of the surrounding cluster and ICM. Top panels show the nuclear region of 3C 196.1 and share the same scale, with a FoV of  $\sim 10 \times 8$  arcsec $^2$  (i.e.  $\sim 30 \times 25$  kpc $^2$ ). *Top Left:* HST/ACS observation of 3C 196.1 from Tremblay et al. (2009), with 8.4 GHz VLA contours superimposed. The HST data have been continuum subtracted, to show only the H $\alpha$ + [N II] emission. The 8.4 GHz contours start at  $\sim 3\sigma$ , i.e. 0.275 mJy, and increase with a square-root scale; the clean beam is ( $0'.3 \times 0'.3$ ,  $0^\circ$ ). The H $\alpha$ + [N II] emission has been aligned with the 8.4 GHz VLA data (shift  $\leq 1'.2$ , see text for details). An H $\alpha$ + [N II] filament extends across the NE radio lobe. The H $\alpha$ + [N II] is aligned with the radio emission (so-called alignment effect, e.g. Baum et al. 1988). *Top Right:* The Chandra 0.7-2 keV emission is shown with the H $\alpha$ + [N II] contours superimposed. No shift was applied to align the images. The Chandra data have  $0'.123$  pixel scale and have been smoothed with a Gaussian kernel of  $1''$ . Depressions in surface brightness are in white. The H $\alpha$ + [N II] contours start at  $0.378 \times 10^{-19}$  erg s $^{-1}$  cm $^{-2}$   $\text{\AA}^{-1}$  and increase with a square-root scale. The SW H $\alpha$ + [N II] emission is bounded to the W, S and SE by regions of low X-ray surface brightness. *Bottom:* The 0.5-10 keV Chandra image, showing an FoV of  $\sim 93 \times 73$  arcsec $^2$  (i.e.  $\sim 297 \times 234$  kpc $^2$ ), with native pixel size. The blue box at the center marks the region of 3C196.1 shown in the top panels. The logarithmic color scale shows the counts per pixel.

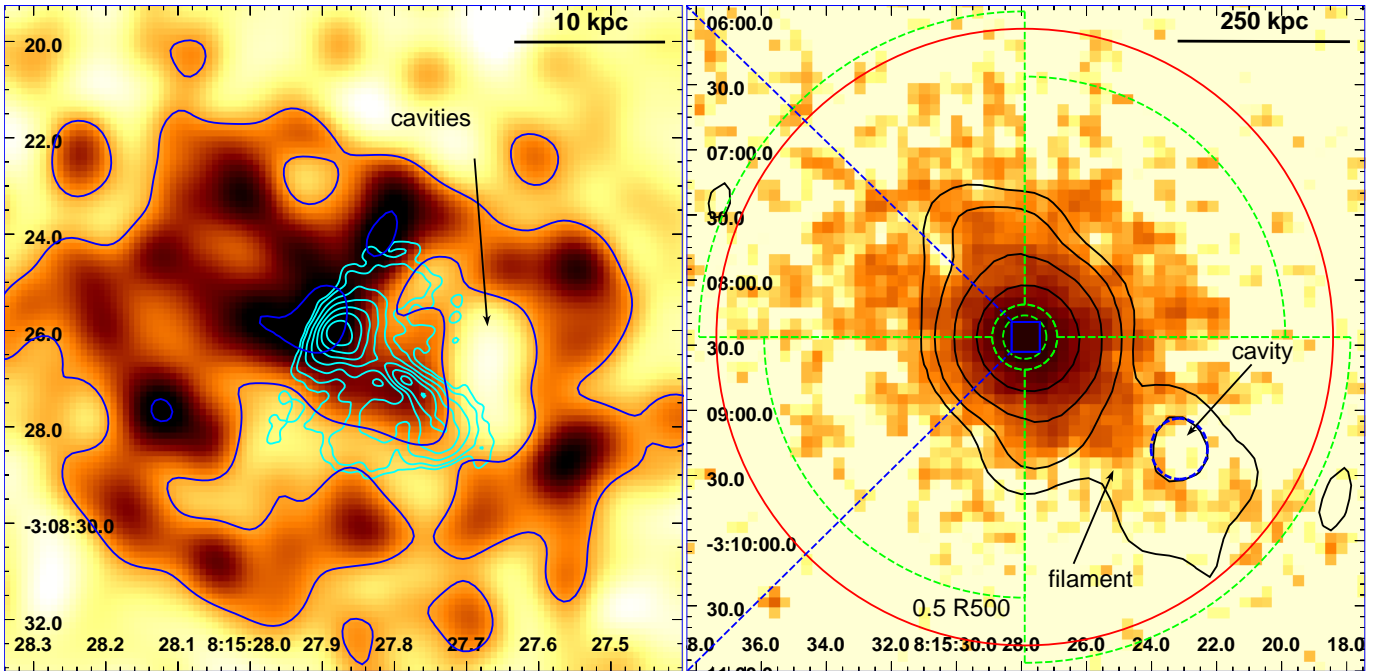


**Figure 2.** *Chandra* 0.7-2 keV energy filtered and point-sources subtracted images of the central BCG 3C 196.1 and of the surrounding cluster and ICM. Regions of low surface brightness are in white. *Left:* Inner  $\sim 13 \times 14$  arcsec<sup>2</sup> (i.e.  $\sim 44 \times 45$  kpc<sup>2</sup>) of the BCG, centered on the brightest X-ray peak. The image is shown with a  $0''.123$  pixel size and has been smoothed with a  $1''$  Gaussian. VLA 8.4 GHz contours are overlaid in cyan (for details see Fig. 1), while the X-ray contours are shown in blue. The lowest blue contour encloses a region of low surface brightness, a “butterfly-shaped” cavity (marked with a black arrow). The brightest X-ray peak is co-spatial with the northern radio lobe and could be a hotspot. *Right:* The BCG and the cluster are shown up to the outskirts, with a FoV of  $\sim 5 \times 5$  arcmin<sup>2</sup> (i.e.  $\sim 960 \times 960$  kpc<sup>2</sup>). Pixel size is  $5''$ , Gaussian smoothing with FWHM= $5''$ . The central blue box is  $\sim 13 \times 14$  arcsec<sup>2</sup> and contains the zoom in shown in the left panel. GMRT 147 MHz contours are overlaid in black starting at  $\sim 3\sigma$ , i.e. 39 mJy with a logarithmic scale. The clean beam is ( $26''.96 \times 25''$ ,  $0^\circ$ ). The arrow marks a large filament which has a projected extension of  $\sim 2'$  (i.e.  $\sim 384$  kpc). It may also be the bottom of a large cavity (highlighted by the dashed blue ellipse), which is co-spatial with the peak of the SW low-frequency diffuse emission. The red circle shows the estimated  $0.5R_{500}$ . Extraction regions used in Sect. 3.2 are shown with green dashed lines.

The optical archival data were observed on 3 December 2006 during Cycle 15 with the Advanced Camera for Surveys (ACS) aboard HST, snapshot program 10882 (PI: Sparks), originally published by Tremblay et al. (2009, we refer the reader to this work for details on data reduction and calibration). The narrowband ACS ramp filter F782N was used to trace the restframe optical  $H\alpha + [N II]$  emission line complex. The HST data have been continuum subtracted to isolate the  $H\alpha + [N II]$  emission. In Fig. 1 we report the central part of the radio galaxy 3C 196.1 imaged with HST/ACS with the high-frequency radio emission at 8.4 GHz superimposed (cyan contours). The HST image was registered in order to align the optical isophotal peak with the southern jet component. The shift of the HST image was  $\lesssim 1''.2$ . The overall  $H\alpha + [N II]$  emission spans  $\sim 10$  kpc projected distance, inside the galaxy, starting from the core and extending along the radio jet. The  $H\alpha + [N II]$  emission is aligned with the 8.4 GHz radio emission. Similar alignments of radio with optical emission lines have been observed in many radio galaxies and is known as “alignment effect”: in powerful radio galaxies, the optical line emitting gas ( $T \sim 10^4$  K

in the proximity of the nuclei has been found to be spatially aligned with the radio jet axes on kpc-scales (Fosbury 1986; Hansen et al. 1987; Baum et al. 1988, 1990; de Vries et al. 1999; Tremblay et al. 2009). The alignment effect is generally explained as due to shocks induced by the jet propagation and by AGN photoionization (Baum & Heckman 1989; Dopita & Sutherland 1995, 1996; Best et al. 2000).

There is also a filament to the NE which drapes across the northern radio lobe. This filamentary structure is not seen in [O III], which shows high-excitation emission in two localized hotspots co-spatial with the elongated bright core (see Fig. 7 in Tremblay et al. 2009).

### 2.3. *Chandra* observation

3C 196.1 was observed during *Chandra* AO12, OBSID 12729 on 11 February 2011, with a nominal 8 ks exposure. The ACIS-S back-illuminated chip was used in VERY FAINT MODE with standard frame times (3.2 s). The source was positioned on ACIS-S3. Data reduction has been performed following the standard reduction procedure described in the *Chandra* Interactive Analysis of Observations (CIAO,

Fruscione et al. 2006) threads<sup>3</sup>, using CIAO v4.9 and the *Chandra* CalDB version 4.7.4. Level 2 event files were generated using the `chandra_repro` task. Events were filtered for grades 0, 2, 3, 4, and 6. The light curve was extracted and checked for high background intervals, the actual live time is 7.93 ks. The resulting 0.5-10 keV *Chandra* image in photon counts with native pixel size is shown in the bottom panel of Fig. 1, in order to show the structures in the original data without any Gaussian smoothing or image processing.

### 3. X-RAY ANALYSIS

#### 3.1. Imaging

Fig. 2 presents the diffuse X-ray emission in the energy range 0.7-2 keV, with pixel size  $0'.123$  (left) and  $5''$  (right). Point sources were detected with the CIAO task `wavdetect` (with 1, 2, 4, 8, 16 and 32 pixels sequence of wavelet scales), adopting a probability of spurious detection of  $10^{-6}$ , and then replaced with local background. Five point sources were detected, all located outside the regions considered in our subsequent analysis. Thus, our results are not affected by the removal of point sources. The images have been smoothed with a Gaussian kernel of  $1''$  (left) and  $5''$  (right). The left panel of Fig. 2 shows the central  $\sim 44 \times 45$  kpc<sup>2</sup> region together with 8.4 GHz contours (cyan) and X-ray contours (blue). The radio source is oriented along the steepest gradient in the X-ray emission. The X-ray surface brightness is complex and is not symmetric, extended along a position angle  $PA^4 \sim 40^\circ$  that matches the optical major axis of the BCG stellar isophotes (see Fig. 32 in de Koff et al. 1996). The image shows the presence of sharp surface brightness edges in the central regions of the cluster. The lowest blue contour marks a system of “butterfly-shaped” surface brightness deficits (see black arrow in Fig. 2), also reported by Massaro et al. (2012) as a “ghost cavity”. The southern jet of the 8.4 GHz source (cyan contours) is bounded (in projection) to the W and E by these “butterfly-shaped” deficits of X-ray radiation. This cavity is mostly devoid of high frequency radio emission. The best description of this source with the available  $0'.3$  resolution is an *hymor* (hybrid morphology radio source Gopal-Krishna & Wiita 2000). The SW side is jet-like (i.e., FR I) whereas the NE side appears to be a classical FR II lobe with a brightness enhancement toward the edge, the X-ray peak marking the location where the NE jet impacts the higher density ICM. Several radio sources have been observed to exhibit a mixed morphology (Kaiser & Best 2007; Kharb et al. 2010; Kapińska et al. 2017), suggesting the FR I/II dichotomy is at least partly due to environmental effects.

On the central panel of Fig. 1 the central region is further magnified, with a field of view (FoV) of  $\sim 30 \times 25$  kpc<sup>2</sup>. The  $H\alpha + [N II]$  emission is overlaid with blue contours. No shift was applied to register the *Chandra* and HST images. The SW optical line emission appears to be confined by the butterfly-shaped X-ray cavity. The  $H\alpha + [N II]$  NE filamentary emission is co-spatial with the northern hotspot.

Also at larger scales, the diffuse X-ray emitting gas distribution is asymmetric, elongated north-east to south-west, as shown in the right panel of Fig. 2, where the system is imaged up to  $\sim 0.5R_{500}$ , with a FoV of  $\sim 1 \times 1$  Mpc<sup>2</sup>. The image shows that the peak of the X-ray emission is centred on the BCG, and that there is a gradient in the surface brightness distribution, with the lowest surface brightness region extending up to few hundreds of kpc. Right panel of Fig. 2 presents low frequency 147 MHz GMRT contours in black. The peak of the low-frequency 147 MHz emission (in the SW extension) is co-spatial with a region of low X-ray surface brightness (see dashed blue ellipse), that could be a large cavity filled with a low-frequency radio bubble. In the outer region there appears an X-ray filament (see black arrow) which has a projected extension of  $\sim 2'$ , corresponding to  $\sim 384$  kpc. It may also outline the southern border of the aforementioned large cavity.

To further explore the underlying physical state of the gas, we derive the temperature in both the nuclear region and the cluster outskirts in Sect. 3.2, and we analyse the surface brightness profiles in Sect. 3.3.

#### 3.2. Spectral analysis

We performed a temperature analysis of the cluster, from the inner core up to  $\sim 0.5R_{500}$ . First we analysed the central core, considering two circles of radius  $r = 10''$  and  $15''$ , both centred on the centroid of the X-ray emission ( $RA_{J2000}=8:15:27.900$  and  $DEC_{J2000}=-3:08:26.265$ ). These two central regions are called *core 0* and *core 1* in Table 1. We then analysed the cluster by dividing the emission into four sectors evenly spanning the 360 degrees. The radial extents of these four regions are  $15''-2'$  for the NW and SE sectors (since in the SE direction the S3 chip ends at that radius) and  $15''-2'.5$  in the NE and SW sectors (see the 6 green dashed regions in the right panel of Fig. 2). We also considered the whole region within  $r = 2'$  to derive the global temperature.

We extracted the spectra in these regions using the CIAO task `specextract`, thereby automating the creation of count-weighted response matrices. Background correction was taken into account using the proper blank sky field event file, which was created using the CIAO task `blanksky`. Background spectra were extracted from the blank sky observation that was re-projected to match the observation. The background-subtracted spectra were then filtered in energy

<sup>3</sup> <http://cxc.harvard.edu/ciao/guides/index.html>

<sup>4</sup> Positive direction is counterclock-wise north through east.

**Table 1.** Results of the spectral fitting analysis of the 0.5–7 keV *Chandra* data. The XSPEC model used is `phabs × APEC`, with  $N_H$  column fixed to Galactic value and  $z$  fixed to 0.198. Prior to extraction, the data were filtered for flaring events, and compact point sources were removed. Spectra were re-binned using a 20-count threshold. Symmetric  $1\sigma$  confidence intervals are shown on fit parameters.

Region [ $r_{in}, r_{out}$ ]	N	$kT$ [keV]	Z [ $Z_{\odot}$ ]	APEC norm [ $10^{-3} \text{cm}^{-5}$ ]	$\chi^2_{\nu}(\nu)$
(1)	(2)	(3)	(4)	(5)	(6)
core 0 [0, 10'']	1115	2.88±0.19	0.80±0.24	1.090±0.090	0.99(44)
		2.81±0.22	0.3 <sup>†</sup>	1.297±0.046	1.13(45)
core 1 [0, 15'']	1534	3.18±0.17	0.98±0.23	1.406±0.097	0.93(57)
		3.14±0.21	0.3 <sup>†</sup>	1.718±0.053	1.16(58)
NW [15'', 2']	809	5.23±0.99	0.24±0.35	0.791±0.075	1.00(33)
		5.24±0.97	0.3 <sup>†</sup>	0.781±0.036	0.97(34)
NE [15'', 2'.5]	959	5.15±0.82	1.12±0.65	0.714±0.080	0.98(39)
		4.85±0.88	0.3 <sup>†</sup>	0.833±0.038	1.02(40)
SE [15'', 2']	590	4.66±0.92	0.99±0.86	0.399±0.063	1.20(25)
		4.37±0.94	0.3 <sup>†</sup>	0.462±0.027	1.20(26)
SW [15'', 2'.5]	1194	7.63±1.80	0.16±0.35	0.975±0.078	0.97(50)
		7.46±1.68	0.3 <sup>†</sup>	0.956±0.035	0.95(51)
All [0, 2']	4228	4.24±0.24	0.73±0.14	4.01±0.14	1.10(154)
		4.25±0.27	0.3 <sup>†</sup>	4.412±0.084	1.16(155)

NOTE—Columns are: (1) extraction region, with range [ $r_{in}, r_{out}$ ], centered at RA<sub>J2000</sub>=8:15:27.900 and DEC<sub>J2000</sub>=-3:08:26.265 (see Fig. 2); (2) net-counts; (3) the best-fit temperature of the APEC model in keV units; (4) the abundance, in solar units; (5) the APEC normalization; (6) the reduced chi square  $\chi^2_{\nu}$ , with the degrees of freedom  $\nu$  in parentheses.

<sup>†</sup> Parameter has been frozen.

between 0.5 and 7 keV, binned using a 20 count threshold and fit using iterative  $\chi^2$  minimization techniques with `xspec` version 12.9.1 (Arnaud 1996).

The model adopted is `phabs × APEC` with column density fixed to the Galactic value  $N_H = 5.81 \times 10^{20} \text{cm}^{-2}$ . We fitted each region twice, first leaving the abundance free to vary and then fixing it to 0.3 times the solar value, which is often found in cluster atmospheres (see e.g. Owers et al. 2009). Abundances were computed taking as reference the solar metallicity as reported by Asplund et al. (2009). Best-fit values are listed in Table 1.

### 3.3. Surface brightness profiles

We extracted surface brightness profiles by considering an azimuthal area up to  $r = 2'$  and again in four sectors with outer radii  $2'$  (NW and SE) or  $2'.5$  (NE and SW). All these five regions were spanned by  $3''$  wide radial bins, apart from the inner core region (up to  $10''$ ) which was divided into  $1''$ -wide bins. In the surface brightness profile analysis, the *Chandra* event file was filtered in energy between 0.7–2 keV band, which is less sensitive to the gas temperature. It was then exposure-corrected, background-subtracted and bright point sources were excluded. The same point sources area was also removed from the blank sky field. Monochromatic exposure maps were computed with nominal energies of 1.35 keV. The background-subtracted and exposure-corrected radial profiles are shown in Fig. 3.

Given the limited counts in our short snapshot observation, we fit the surface brightness profiles at projected distance  $r$  with a  $\beta$ -model (Cavaliere & Fusco-Femiano 1976)

$$S(r) = S_0 \left[ 1 + \left( \frac{r}{r_c} \right)^2 \right]^{-3\beta+0.5}, \quad (1)$$

where  $S_0$  is the central X-ray surface brightness and  $r_c$  is the core radius. We adopted the IDL package `MPFIT` (Markwardt 2009), which uses the Levenberg-Marquardt technique to determine the least-squares best fit. Best-fit models are reported as red solid curves in Fig. 3, together with best-fit parameters. Residuals are shown in the lower panels of Fig. 3.

The F-test was then carried out in order to quantitatively verify whether a two  $\beta$ -model<sup>5</sup> was to be preferred, adopting a significance threshold of 0.05. The two  $\beta$ -model was always rejected, with the exception of the SW sector.

The ICM in galaxy clusters is typically well fitted by models with  $\beta \sim 0.6$  (Sarazin 1986; Ettori & Balestra 2009), which steepens with increasing core radius as the two parameters are strongly correlated (Morandi et al. 2015). Our results are in good agreement, as we find that the average surface brightness (azimuthally extracted up to  $2'$ ) is well fitted by a single  $\beta$ -model with  $\beta = 0.51 \pm 0.01$ . The other three sectors give a rather consistent picture, with  $\beta$  ranging from  $0.47 \pm 0.01$  in the NE sector to  $0.56 \pm 0.02$  in the SE sector. To properly fit the SW profile, we fixed the core radius to  $r_{c,1} \sim 15$  kpc (as found from the average azimuthal fit) and  $r_{c,2} \sim 135$  kpc, and the resulting best-fitting slopes are:  $\beta_1 = 0.56 \pm 0.02$ , consistent with the fit results of the other four regions, and  $\beta_2 = 1.1 \pm 0.1$ .

The surface brightness profile, closely tracing the underlying 3-d distribution of the gas density, should strictly follow an isothermal profile. Thus a small deviation from the the-

<sup>5</sup> A two  $\beta$ -model is defined as the linear combination of two different  $\beta$ -models as given in eq. 1.

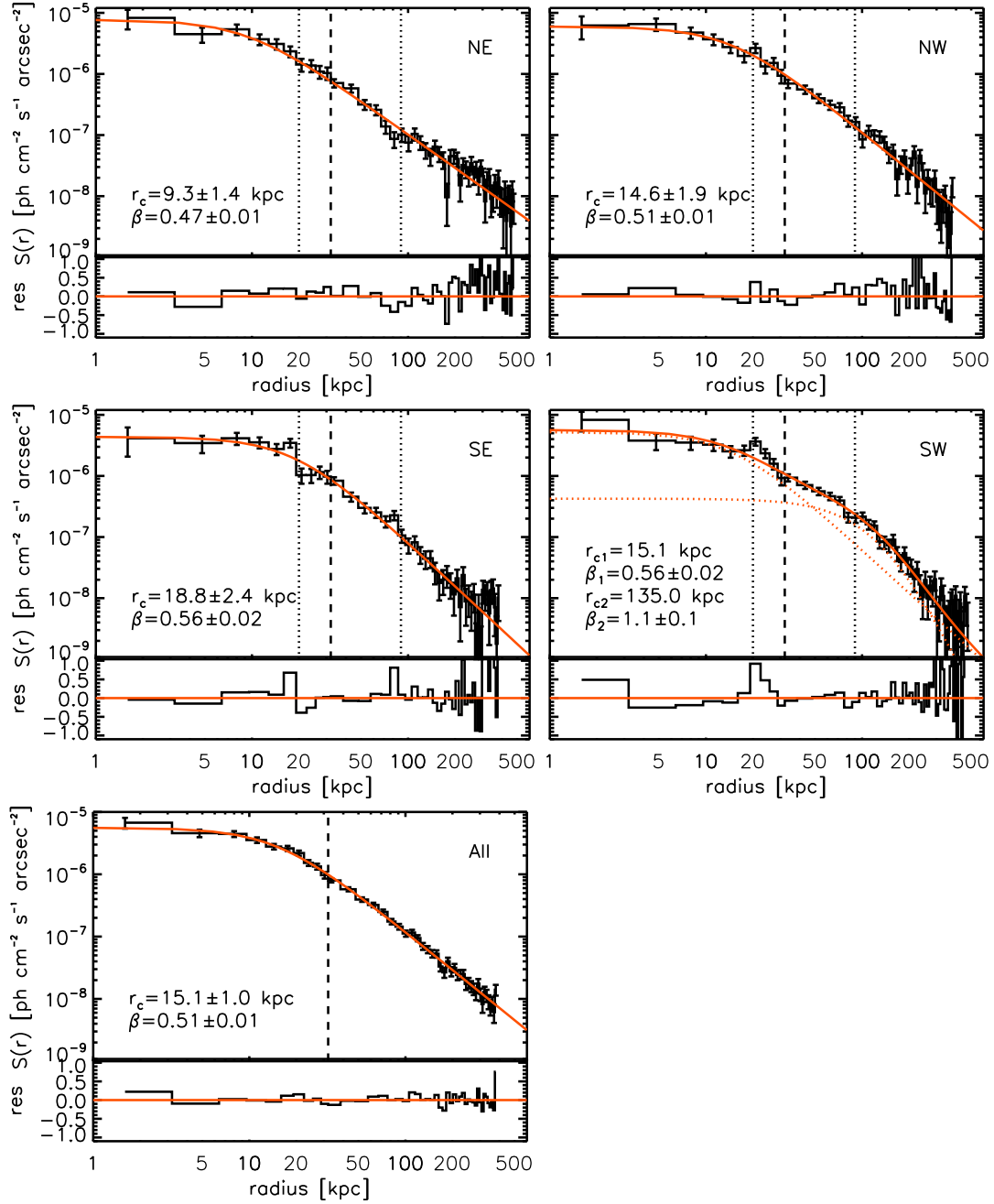


**Figure 3.** Exposure-corrected and background-subtracted surface brightness profiles of four sectors, evenly spanning the 360 degree, and of an azimuthal region, extending up to  $2'$ . Bright point sources were excluded. Radial bins are  $3''$  wide, with the exception of the inner  $10''$ , which were spanned by  $1''$ -bins. The radial profiles have been computed in 0.7-2 keV band, which is less sensitive to the temperature. Parameters of the  $\beta$ -models are also reported. The dashed line marks the inner core region  $r = 10''$ , which has a lower temperature of  $\sim 3$  keV (see region *core 0* in Table 1). The dotted lines show the location of possible density jumps, reflected as change of slopes in the surface brightness profiles. Lower panels show the residuals of the fit.

oretical profile, visible as a change of slope in the surface brightness radial profile, reflects a discontinuity in the underlying gas density. The surface brightness profiles plotted in Fig. 3 indeed show these changes of slopes, marked with dotted lines, at  $\sim 20$  kpc, which were already visible as sharp surface brightness “edges” in the central  $44 \times 45$  kpc<sup>2</sup> FoV in Fig. 2, left panel. There is a discontinuity in the slope of the surface brightness radial profile also in the outer region, around  $\sim 90$  kpc, that was not evident in Fig. 2.

To constrain the discontinuity conditions, in the most discrepant cases, e.g. NE and SE, we fit the surface brightness profile within each region assuming spherical symmetry for the gas density and constant gas temperature. The significance of the density discontinuity was quantified by modelling the surface brightness profile across the contact discontinuity with a broken power law density model (see Appendix of Owers et al. 2009). Given the limited counts of our snapshot observation, we fix the location of the density discontinuity to help the fitting minimization procedure.

For temperatures greater than 2 keV, the discontinuity in the slope of the surface brightness profile is related to the discontinuity in the gas density as

$$\frac{n_{e,1}}{n_{e,2}} \approx \sqrt{\frac{S_1}{S_2}}, \quad (2)$$

where  $n_{e,1}$ ,  $n_{e,2}$  are the densities on either side of the edge, and  $S_1$ ,  $S_2$  are the amplitudes of the corresponding surface brightness values. These profiles reveal density ratios of  $1.61 \pm 0.51$  at a distance of 21 kpc, and  $1.77 \pm 0.30$  at a distance of 90 kpc in the SE sector, and  $1.80 \pm 0.27$  at distance of 85 kpc in the NE region. The position of the outer jumps are quite symmetric between the two sides, since they are at 90 and 85 kpc SE and NE respectively. Assuming the density discontinuities are associated with shocks, the Mach number  $\mathcal{M}$  is given by the Rankine-Hugoniot jump condition:

$$\frac{n_{e,d}}{n_{e,u}} = \frac{\gamma + 1}{\gamma - 1 + 2\mathcal{M}^{-2}} \quad (3)$$

where  $n_{e,d}$  and  $n_{e,u}$  are the densities downstream and upstream of the shock, respectively. Assuming an ideal gas with ratio of specific heats  $\gamma = 5/3$  and the density ratios measured above, the resulting Mach numbers are:  $\mathcal{M} = 1.42 \pm 0.38$  (SE,  $r=21$  kpc);  $\mathcal{M} = 1.54 \pm 0.24$  (SE,  $r=85$  kpc);  $\mathcal{M} = 1.57 \pm 0.22$  (NE,  $r=90$  kpc); which are consistent with a shock origin. We note that by estimating the Mach numbers from the density jumps as shown in eq. 3, we are assuming they are due to shocks. However, it could be that these density discontinuities are caused by sloshing fronts, in which case the temperature discontinuity would be the reciprocal of the density jump. Deeper X-ray observations would certainly clarify what is the physical origin of the discontinuities.

### 3.4. Cavities, Asymmetries and Spiral features

Surface brightness edges may be caused by at least three phenomena: cold fronts, sloshing of the gas in the central regions of clusters induced by minor mergers, and shocks either AGN- or merger-driven. In particular, gas sloshing is signalled by the presence of a spiral structure in the hot gas distribution (Markevitch & Vikhlinin 2007). To further enhance small amplitude features in the surface brightness, that are otherwise overwhelmed by the gradient associated with the cluster, we adopt two edge-enhancement methods, presented in Fig. 4. We caution the reader to not over-interpret the structures in Fig. 4. Indeed, the two edge-enhancement methods adopted are inherently noisy, and introduce artefacts that complicate quantitative morphological analysis. Fig. 4 (particularly the rightmost panel) is presented mostly as a viewing aid for the major morphological features, which are (almost) already visible from the unprocessed data shown in Fig. 2.

To highlight the small-scale ripples in the surface brightness, searching for cavities, edges and sloshing features, we produced a residual image by subtracting a 2D elliptical  $\beta$ -model from the 0.7-2 keV *Chandra* image after excising the point sources (see Sect. 3.1), with native pixel scale  $0''.492$ , up to  $2'$ . The left panel of Fig. 4 shows the residual image, where regions of surface brightness excess over the subtracted  $\beta$ -model appear in black, whereas deficits are shown in white. The left panel shows the central  $20 \times 25$  arcsec<sup>2</sup> ( $65 \times 80$  kpc<sup>2</sup>) residual image. The butterfly-shaped cavity is clearly seen as a deficit in the residuals. The dark sharp region surrounding the cavity to the W, S and SE is seen as an excess. This edge has a projected radial extent of  $\sim 10$  kpc ( $\sim 3''$ ) with the outer border at a distance of  $\sim 20$  kpc. This is consistent with the first discontinuity in the slope of the surface brightness radial profiles (see dotted lines at  $\sim 20$  kpc in Fig. 3).

The central panel shows a larger region, with a FoV of  $\sim 1 \times 1.5$  arcmin<sup>2</sup> ( $\sim 215 \times 290$  kpc<sup>2</sup>). Pixel scale is  $0''.492$ , smoothed with a Gaussian kernel of  $10''$ . The Gaussian-smoothed residual image shows asymmetries in the surface brightness. Residuals asymmetric features are expected in case of gas sloshing, and indeed a spiral feature indicative of sloshing is clearly evident both as excess emission (W and S, dark) and deficit (E and N, white). The dark spiral arm is  $\sim 6''$  wide and  $\sim 12''$  long, which means  $\sim 20 \times 40$  kpc<sup>2</sup>.

We also employed an unsharp mask procedure, which is usually adopted as a bandpass spatial filter, in order to enhance structures between the desired spatial scales. The 0.7-2 keV point-source subtracted image is convolved with Gaussian kernels of different sizes. We adopted the kernels of  $15''$  and  $30''$  to highlight the underlying density discontinuity at  $\sim 90$  kpc indicated by the change of slope in the surface brightness radial profiles in Fig. 3. The 30-arcsec smoothed

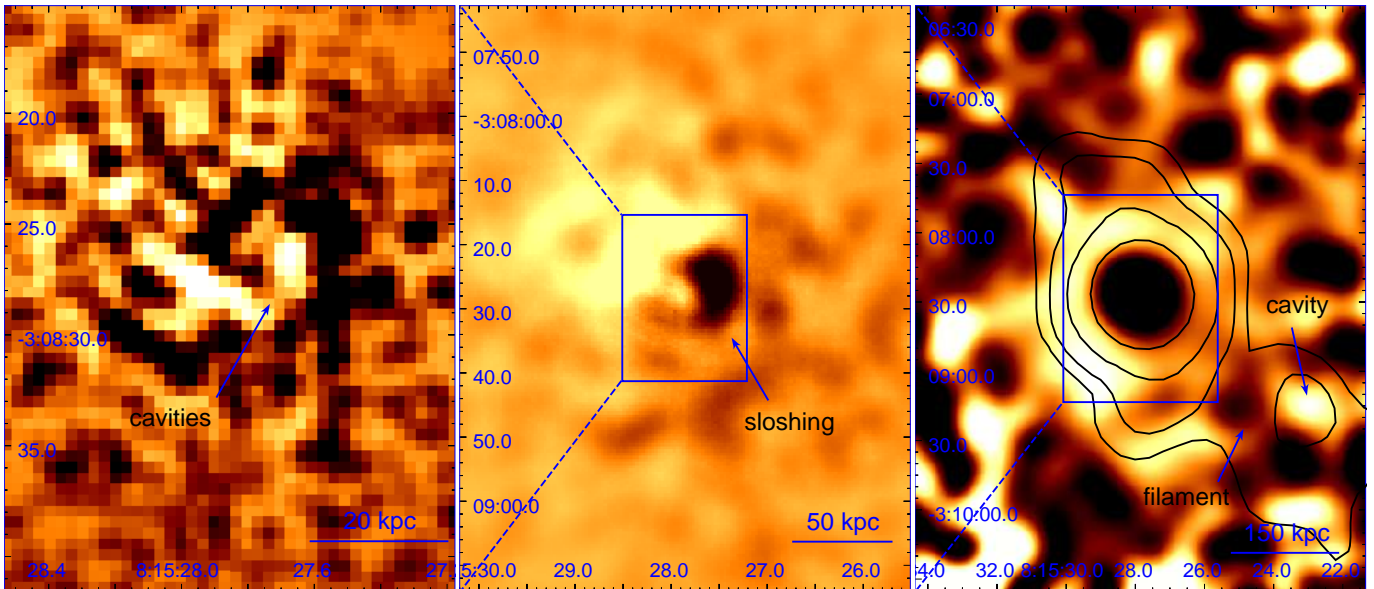


**Figure 4.** Residuals images of the 0.7-2 keV energy band, with  $0''.492$  pixel scale. Excess emission appears in black while depressions are shown in white. *Left:* Residual image produced by the subtraction of a  $\beta$ -model, FoV is  $20 \times 25$  arcsec $^2$  ( $65 \times 80$  kpc $^2$ ). The butterfly-shaped cavity is clearly seen in the residuals, together with a dark sharp shell that surrounds it. This dark edge is  $\sim 10$  kpc long in projection. *Center:* The same image is smoothed with a 10-arcsec Gaussian kernel. FoV is  $\sim 1 \times 1.5$  arcmin $^2$ . Asymmetries in the surface brightness are seen together with a spiral feature, indicative of gas sloshing. *Right:* Unsharp mask image produced by the subtraction of 30-arcsec smoothed image from the 15-arcsec smoothed image. The subtracted data are then divided by the sum of the two smoothed images. Field of view is  $3 \times 4$  arcmin $^2$ . GMRT 147 MHz contours are overplotted in black (see Fig. 2 for details). This edge-enhancement method highlights both the outer cavity, co-spatial with the low-frequency radio emission, and the surrounding filament.

image is subtracted from the 15-arcsec smoothed image and then the subtracted data are divided by the sum of the two images. The right panel of Fig. 4 shows the resulting unsharp mask image together with the GMRT 147 MHz contours overlaid in black. The FoV is  $3 \times 4$  arcmin $^2$ . Asymmetries in the surface brightness are enhanced even at such scales. The large outer cavity mentioned in Fig. 2 is clearly seen in this unsharp masked image, as indicated by the arrow in Fig. 4, as well as the filament that surrounds this cavity.

## 4. RESULTS

### 4.1. Temperature gradient

The spectral analysis performed on the *Chandra* data outlined in Sect. 3.2 implies that the cluster is well fitted by an APEC plasma having  $\sim 4.2$  keV temperature. Inverting the  $M_{500} - T$  relation of Lovisari et al. (2015), this temperature corresponds to an  $R_{500} \approx 0.9$  Mpc, which is consistent with the estimate reported by Piffaretti et al. (2011). The temperature analysis shows that the region called *core 1* in Table 1 has a cooler temperature of  $\sim 3.2$  keV. The best-fit gas temperature further drops in the region *core 0*, i.e. considering only the central  $10''$ , to  $\sim 2.8$  keV.<sup>6</sup> In the four outer sectors (NW, NE, SE, SW), the best-fit temperatures are higher

<sup>6</sup> The difference between the two core best-fit temperatures is statistically marginal,  $\sim 1\sigma$ .

(at  $\geq 2\sigma$  with respect to the region *core 0*). This result suggests that the cluster could be a cool core cluster, with a lower temperature in the central region with respect to the peripheral zones. In the SW direction (coincident with the low-frequency 147 MHz peak emission) there is a hint of a rise in the gas temperature ( $\sim 7.5$  keV, see Table 1) with respect to the other three regions. However this rise in the SW is not statistically significant ( $\lesssim 1.5\sigma$ ), due to the large uncertainties in the best-fit gas temperatures in the cluster outskirts. Indeed, the *Chandra* image has insufficient counts to accurately constrain the temperature in the cluster outskirts, with current  $1-\sigma$  uncertainties of  $\sim 20\%$ .

### 4.2. Central density, entropy and cooling time

Under the assumption of spherical symmetry and that the projected 2D surface brightness can be described by a  $\beta$ -model (see Sect. 3.3), we can derive the underlying 3D electron gas density distribution

$$n_e(r) = n_{e,0} \left[ 1 + \left( \frac{r}{r_c} \right)^2 \right]^{-\frac{3}{2}\beta}. \quad (4)$$

The central electron density  $n_{e,0}$  is obtained using the spectral fit. When fitting a spectrum with an APEC model, the normalization  $K$  gives us the electron  $n_e$  and proton densities  $n_p$

$$K = \frac{10^{-14}}{4\pi D_A^2 (1+z)^2} \int n_e(r) n_p(r) dV, \quad (5)$$

where  $D_A$  is the source angular distance. The normalization in equation 5 is computed in the volume  $dV$  through an infinite cylinder, first integrating radially up to the extraction radius, and then between  $-\infty$  and  $\infty$  in order to consider all the emission along the line of sight. Assuming a fully ionized gas,  $n_p \approx 0.82n_e$ , we can recover the gas density. The average central density, estimated from the best-fitting parameters of the  $\beta$ -model describing the azimuthal profile inside  $2'$  (see bottom-panel of Fig. 3), is  $n_{e,0} \approx 0.098 \text{ cm}^{-3}$ .

We can now estimate the core entropy index, which is defined as  $T/n_e^{2/3}$ , with the temperature in keV units and the density measured in  $\text{cm}^{-3}$ . The entropy can be uniquely determined from the entropy index. We use the average temperature of the central region *core 0*, i.e.  $kT(r < 10'') \approx 2.8 \text{ keV}$ , and the aforementioned estimate of the central density  $n_{e,0}$ . The resulting core central entropy index is  $\sim 13 \text{ keV cm}^2$ , and thus the system fits the definition of cool core cluster, taking the characteristic dividing line at  $\sim 25 \text{ keV cm}^2$  (Hudson et al. 2010). A low central entropy index value is supported by our analysis which pinpoints a variety of multiphase gas. Indeed, multiphase gas and star formation activity, as hinted for instance by the H $\alpha$  emission (see Fig. 1), is expected to be enhanced in BCGs that harbour radio galaxies and with central entropy index below  $30 \text{ keV cm}^2$  (Cavagnolo et al. 2008). However, note that the position of the AGN is not obvious so its contribution to the X-ray emission cannot be subtracted resulting in an overestimate of the X-ray emission, and consequently the central density and entropy. The flux from the cool core contained within  $0.15R_{500}$  is  $\sim 1.5 \times 10^{-12} \text{ erg cm}^{-2} \text{ s}^{-1}$  in the 0.1-2.4 keV band, corresponding to a luminosity of  $\sim 1.5 \times 10^{44} \text{ erg s}^{-1}$ . The upper limit on the X-ray nuclear flux (observed-frame and uncorrected for absorption), computed considering all the emission coming from the central circle with radius  $2''$ , is  $\sim 3 \times 10^{-15} \text{ erg cm}^{-2} \text{ s}^{-1}$  in the soft 0.5-1 keV and medium 1-2 keV bands, and  $\sim 7 \times 10^{-15} \text{ erg cm}^{-2} \text{ s}^{-1}$  in the hard 2-7 keV band. Nonetheless, the galaxy is classified in the optical as a LERG (Buttiglione et al. 2010), and as such the X-ray emission from the accretion disk is expected to be low (e.g., Hardcastle et al. 2009), hence the AGN X-ray contribution probably does not affect much our results.

Additional evidence for a cool core cluster is given by the cooling time

$$t_{cool} = \frac{3(n_e + n_p)kT}{2\Lambda(T, Z)n_en_p} \quad (6)$$

where  $\Lambda(T, Z)$  is the so-called cooling function, which can be estimated using XSPEC. We found that  $\Lambda(kT = 2.8 \text{ keV}, Z = 0.3) \approx 1 \times 10^{-23} \text{ erg cm}^3 \text{ s}^{-1}$ , which gives a cooling time  $t_{cool} \sim 5 \times 10^8 \text{ yr}$  (assuming an APEC model with best-fit parameters obtained for the region *core 0*, with 0.3 solar abundance, and a fully ionized gas). The age of the Universe at redshift 0.198 is  $t_{age} = 11.122 \times 10^9 \text{ yr}$ , thus  $t_{cool}/t_{age} < 0.05$

supports the cool core nature of the cluster.

### 4.3. Cavities energetics and age

Fig. 2 shows the 8 ks *Chandra* snapshot observation and the 8.4 GHz radio contours of the core region. There is a wealth of structures already in the snapshot observation, which suggests a complex dynamical state of the system, that could have experienced multiple AGN outbursts. The luminosity  $L_{500}$  extrapolated up to  $R_{500}$  in the 0.1-2.4 keV band is  $\sim 2.8 \times 10^{44} \text{ erg s}^{-1}$ , which is consistent with the *ROSAT* measurement (Piffaretti et al. 2011). As already introduced in Sect. 3.1, in the inner region there is a ‘‘butterfly-shaped’’ cavity wrapping around the SW jet/lobe. The steep (radio) spectrum ‘‘S-lobe’’ impinges on part of this cavity. This system of cavities can be approximated as two contiguous ellipsoids, at a distance  $\sim 10 \text{ kpc}$  ( $\approx 3''$ ), each with a semi-major axis of  $2''$  and a semi-minor axis of  $1''$ . To compute the volume we will assume that the semi-axis along the line of sight is the average of the two, i.e.  $1''.5$ . The resulting volume of each ellipsoid is  $1.2 \times 10^{67} \text{ cm}^3$ , corresponding to a total cavity volume of  $\sim 820 \text{ kpc}^3$ .

On large scales, the low-frequency 147 MHz emission extends for hundreds of kpc to the SW. As already discussed in Sect. 3.1, this low-frequency radio emission is aligned with the inner scale jet emission. As highlighted in Fig. 2 there is a large X-ray filament extending towards the south-west, which spans  $\sim 2'$  ( $\sim 384 \text{ kpc}$ , projected). It could also be the southern border of a large cavity in the hot gas, appearing as a deficit in the X-ray surface brightness, which is co-spatial with the peak of 147 MHz radio emission (see Fig. 2, right panel). This cavity is marked by a blue dashed ellipsoid with semi-major axis  $14''$  and semi-minor axis  $13''$  (the semi axis along the line of sight is taken  $13''.5$ ). The centre of this ellipsoid lies at a (projected) distance of  $\sim 90''$  from the AGN. The volume of this cavity would be  $\sim 10^{70} \text{ cm}^3$ , corresponding roughly to  $3 \times 10^5 \text{ kpc}^3$ . In both cases, the estimated cavity volumes do not take into account any effect of projection, therefore they should be considered as upper limits on the real cavity volume. Also, the choice of the semi axis along the line of sight is arbitrary, even though it is consistent with the standard approximation usually adopted in the literature.

The pressure associated with each cavity is given by  $P_{cav} = (n_e + n_p)kT \approx 1.82n_e(r)kT(r)$ . By assuming that: i) the electron density is described by the  $\beta$ -model parameters derived from the azimuthal fit of the region contained in  $2'$  (see Fig. 3); ii) a fully ionised gas; and iii) taking  $kT=2.8 \text{ keV}$  as determined by the spectral fitting in the central  $10''$  region (see Table 1) for the inner cavity and instead  $kT=4.2 \text{ keV}$  for the cavity that is located at  $\sim 90''$ ; the resulting pressures

are  $P_{cav}^{in} \simeq 0.5 \text{ keV cm}^{-3}$  for the butterfly-shaped cavity and  $P_{cav}^{out} \simeq 0.05 \text{ keV cm}^{-3}$  for the outer cavity.

Assuming a relativistic plasma, the minimum energy required to create a cavity, e.g. the cavity enthalpy, is

$$E_{cav} = \frac{\gamma}{\gamma - 1} P_{cav} V = 4P_{cav} V \quad (7)$$

which is  $\sim 7 \times 10^{58}$  erg for the inner cavity and  $\sim 3 \times 10^{60}$  erg for the outer cavity.

If the low frequency radio emission comes from a buoyantly rising radio lobe that originated in a past AGN outburst and has displaced the X-ray emitting gas, we can compute its age given its projected cluster-centric distance  $R \sim 90''$  ( $\sim 290$  kpc). Assuming the bubble is launched from the nucleus and rises in the plane of the sky at the sound speed  $c_s$  (see e.g. the review from McNamara & Nulsen 2007)

$$c_s = \sqrt{\frac{kT}{\mu m_p}} \simeq 1100 \left( \frac{kT}{5 \text{ keV}} \right)^{1/2} \text{ km s}^{-1} \quad (8)$$

where  $\mu = 0.62$  is the mean molecular weight in units of the proton mass  $m_p$ , and that the ambient temperature at distance  $R$  is  $kT(R) = 4.2$  keV, then the age of this radio emitting plasma would be

$$t_{rise} \simeq R/c_s = 280 \text{ Myr}. \quad (9)$$

The simple assumption of a sonic expansion of the bubble does not consider an evolution in the bubble velocity, where the initial stages of the cavity inflation are usually thought to be supersonic and then followed by subsonic buoyant rise. Nonetheless, eq. 9 represents a simple approach that can be used to get an estimate of age average between the two inflation phases.

The age of this radio emission should be of the same order as the AGN radio phase, if this radio emission is related to previous radio outbursts. A timescale of  $\sim 10^8$  yr is indeed consistent with cycling times between the triggering of radio activity, the onset of quiescence and the subsequent re-ignition of activity, e.g.  $10^7$ - $10^8$  yr (Parma et al. 1999; Best et al. 2005; Shabala et al. 2008; Tremblay et al. 2010). In general, synchrotron losses limit radio source lifetimes to  $\sim 10^8$  yr in a few  $\mu\text{G}$  magnetic field typical of lobes in radio galaxies, unless there has been re-acceleration of the electron population.

We can estimate the same quantities also for the inner cavity, at a distance of  $\sim 10$  kpc, assuming that the temperature inside the cavity is given by the average temperature  $kT \sim 2.8$  keV we found in the region *core 0*. We then get an age of  $\sim 12$  Myrs.

We can finally compute the jet power  $P_{jet}$ , which is the minimum work required to inflate a cavity with a volume  $V$ , i.e. the cavity enthalpy in eq. 7, divided by the age of the

cavity,

$$P_{jet} = 4PV/t = E_{cav}/t. \quad (10)$$

As shown in eq. 9, the cavity age can be approximated by the bubble rise time, under the (simplistic) assumption of sonic expansion. The resulting jet powers are  $\sim 1.9 \times 10^{44}$  erg  $\text{s}^{-1}$  for the inner cavity and  $\sim 3.4 \times 10^{44}$  erg  $\text{s}^{-1}$ , which are consistently measured also in other galaxy clusters (see the review of Bykov et al. 2015, their Fig. 7).

## 5. SUMMARY AND CONCLUSIONS

Performing a multi-wavelength analysis from publicly available radio, optical and X-ray images, we have investigated the nature of the multiphase emitting gas both in the nuclear and surrounding regions of 3C 196.1. The emerging scenario is that this radio galaxy could have undergone several radio outbursts on multiple epochs and its cluster may have experienced a merger. In particular:

1. Optical HST observations reveal clear signs of interactions between the radio jet and lobe with the  $\text{H}\alpha$ + $[\text{N II}]$  emitting gas. Distortions in the optical isophotes of the BCG support a scenario of merging. In Fig. 1 there is filamentary  $\text{H}\alpha$ + $[\text{N II}]$  emission extending eastwards, draped across the radio lobe. This  $\text{H}\alpha$ + $[\text{N II}]$  filament must be dynamically very short lived. Indeed, recombination times for  $T \sim 10^4$  K gas are of order  $10^3$  yr (Osterbrock & Ferland 2006), while lifetimes of radio sources are of order  $10^8$  yr. The process by which the  $\text{H}\alpha$ + $[\text{N II}]$  gas is ionized should therefore be ongoing throughout the lifetime of the radio source. This implies a strong connection between AGN activity and observed emission line properties;
2. The low-frequency and high-frequency radio data helped us to investigate both the inner and outer scale of the cluster. By comparing the galactic-scale radio and HST images, we have found that the  $\text{H}\alpha$ + $[\text{N II}]$  emission is aligned with the inner scale jet, an example of the well-known ‘‘alignment effect’’ (Fosbury 1986; Hansen et al. 1987; Baum et al. 1988, 1990; de Vries et al. 1999; Tremblay et al. 2009). The combination of the radio and the X-ray images allowed us to discover cavities located in the galaxy, at  $\sim 10$  kpc, and in the cluster outskirts, at  $\sim 290$  kpc, whose presence suggests past AGN outbursts;
3. The  $\text{H}\alpha$ + $[\text{N II}]$  emission is bounded to the SW by the butterfly-shaped cavity in the inner region and the filamentary emission to the NE is co-spatial with the northern hotspot;
4. The *Chandra* X-ray data analysis allowed us to constrain basic physical parameters of the cluster and of

the ICM gas. We revealed the presence of discontinuities in the gas density by analysing the surface brightness profiles. Assuming these discontinuities are due to shocks, we determined the Mach numbers from the density jumps, derived under the Rankine-Hugoniot conditions. The inferred Mach numbers and density jumps are consistent with being originated by shocks. We also employed two different edge-enhancement methods to better visualize the small ripples in surface brightness associated with density discontinuities. In this way we found a spiral pattern, characteristic of gas sloshing, suggesting a past merger event;

5. We found a decrease in temperature in the inner region, suggesting that 3C 196.1 is hosted in a cool core cluster. This result is further supported by the analysis of the X-ray surface brightness, through which we determined the core entropy index of  $\sim 13 \text{ keV cm}^2$  and the cooling time  $t_{cool} \sim 500 \text{ Myrs}$ ;
6. Finally we computed the volumes, pressures and enthalpies  $E_{cav}$  associated with the cavities:  $E_{cav} \sim 7 \times 10^{58} \text{ erg}$  for the inner cavity and  $E_{cav} \sim 3 \times 10^{60} \text{ erg}$  for the outer cavity. We also determined the lifetimes of both cavities, the inner cavity of  $\sim 12 \text{ Myrs}$  and the outer one of  $\sim 280 \text{ Myrs}$ , by assuming that the radio plasma is a sonic rising bubble. This lifetime is consistent with radio cycle lifetimes and thus supports the origin of the outer cavity as a past AGN outburst. With the estimate of bubble rise time, we computed the jet powers  $P_{jet}$  and found  $P_{jet} \sim 1.9 \times 10^{44} \text{ erg s}^{-1}$  for the inner cavity and  $P_{jet} \sim 3.4 \times 10^{44} \text{ erg s}^{-1}$  for the outer cavity.

Given that the  $\text{H}\alpha + [\text{N II}]$  gas filaments are aligned with the radio jets/bubbles, we are probably witnessing an example here of lobes uplifting cold gas, even though robust conclusions cannot be drawn since we do not have any kinematic information. Deeper X-ray and radio data would be critical to provide clues about the dynamics of the cold and hot phase gas, and to obtain a more complete understanding of the morphology and of the nature of the system. Additional

deeper data would be also needed to better define cavities, constrain the temperature and metallicity distributions, and look for additional merger features. This source thus represents an intriguing opportunity to quantify, with deeper X-ray observations, the impact of AGN activity in the outskirts of a group in a nearby cluster.

We thank the referee for valuable suggestions that improved the quality of the manuscript. We acknowledge C. C. Cheung for kindly providing the 8.4 GHz radio map. This investigation is supported by the National Aeronautics and Space Administration (NASA) grants GO4-15096X, GO4-15097X and GO6-17081X. FR acknowledges support from FONDECYT Postdoctorado 3180506 and CONICYT Chile grant Basal-CATA PFB-06/2007. LL acknowledges support from NASA through contract NNX17AD83G. This work is supported by the "Departments of Excellence 2018 - 2022" Grant awarded by the Italian Ministry of Education, University and Research (MIUR) (L. 232/2016). This research has made use of resources provided by the Compagnia di San Paolo for the grant awarded on the BLENV project (S1618\_L1\_MASF\_01) and by the Ministry of Education, Universities and Research for the grant MASF\_FFABR\_17\_01. FM acknowledges financial contribution from the agreement ASI-INAF n.2017-14-H.0. The work of SB and CO was supported by NSERC (Natural Sciences and Engineering Research Council of Canada). This research has made use of NASA's Astrophysics Data System; SAOImage DS9, developed by the Smithsonian Astrophysical Observatory, and the NASA/IPAC Extragalactic Database (NED), which is operated by the Jet Propulsion Laboratory, California Institute of Technology, under contract with the National Aeronautics and Space Administration. The (USA) National Radio Astronomy Observatory (NRAO) is operated by Associated Universities, Inc. and is a Facility of the (USA) National Science Foundation. We thank the staff of the GMRT that made these observations possible. GMRT is run by the National Centre for Radio Astrophysics of the Tata Institute of Fundamental Research. Facilities: VLA, GMRT, HST, CXO (ACIS).

## REFERENCES

- Arnaud, K. A. 1996, in *Astronomical Society of the Pacific Conference Series*, Vol. 101, *Astronomical Data Analysis Software and Systems V*, ed. G. H. Jacoby & J. Barnes, 17
- Asplund, M., Grevesse, N., Sauval, A. J., & Scott, P. 2009, *ARA&A*, 47, 481, doi: [10.1146/annurev.astro.46.060407.145222](https://doi.org/10.1146/annurev.astro.46.060407.145222)
- Baum, S. A., & Heckman, T. 1989, *ApJ*, 336, 681, doi: [10.1086/167043](https://doi.org/10.1086/167043)
- Baum, S. A., Heckman, T., & van Breugel, W. 1990, *ApJS*, 74, 389, doi: [10.1086/191504](https://doi.org/10.1086/191504)
- Baum, S. A., Heckman, T. M., Bridle, A., van Breugel, W. J. M., & Miley, G. K. 1988, *ApJS*, 68, 643, doi: [10.1086/191301](https://doi.org/10.1086/191301)
- Begelman, M. C., & Nath, B. B. 2005, *MNRAS*, 361, 1387, doi: [10.1111/j.1365-2966.2005.09249.x](https://doi.org/10.1111/j.1365-2966.2005.09249.x)
- Bennett, A. S. 1962, *MNRAS*, 125, 75, doi: [10.1093/mnras/125.1.75](https://doi.org/10.1093/mnras/125.1.75)

- Best, P. N., Kauffmann, G., Heckman, T. M., & Ivezić, Ž. 2005, *MNRAS*, 362, 9, doi: [10.1111/j.1365-2966.2005.09283.x](https://doi.org/10.1111/j.1365-2966.2005.09283.x)
- Best, P. N., Röttgering, H. J. A., & Longair, M. S. 2000, *MNRAS*, 311, 23, doi: [10.1046/j.1365-8711.2000.03028.x](https://doi.org/10.1046/j.1365-8711.2000.03028.x)
- Birzan, L., McNamara, B. R., Nulsen, P. E. J., Carilli, C. L., & Wise, M. W. 2008, *ApJ*, 686, 859, doi: [10.1086/591416](https://doi.org/10.1086/591416)
- Blanton, E. L., Randall, S. W., Clarke, T. E., et al. 2011, *ApJ*, 737, 99, doi: [10.1088/0004-637X/737/2/99](https://doi.org/10.1088/0004-637X/737/2/99)
- Boehringer, H., Voges, W., Fabian, A. C., Edge, A. C., & Neumann, D. M. 1993, *MNRAS*, 264, L25, doi: [10.1093/mnras/264.1.L25](https://doi.org/10.1093/mnras/264.1.L25)
- Buttiglione, S., Capetti, A., Celotti, A., et al. 2010, *A&A*, 509, A6, doi: [10.1051/0004-6361/200913290](https://doi.org/10.1051/0004-6361/200913290)
- Bykov, A. M., Churazov, E. M., Ferrari, C., et al. 2015, *SSRv*, 188, 141, doi: [10.1007/s11214-014-0129-4](https://doi.org/10.1007/s11214-014-0129-4)
- Cavagnolo, K. W., Donahue, M., Voit, G. M., & Sun, M. 2008, *ApJL*, 683, L107, doi: [10.1086/591665](https://doi.org/10.1086/591665)
- Cavagnolo, K. W., McNamara, B. R., Nulsen, P. E. J., et al. 2010, *ApJ*, 720, 1066, doi: [10.1088/0004-637X/720/2/1066](https://doi.org/10.1088/0004-637X/720/2/1066)
- Cavaliere, A., & Fusco-Femiano, R. 1976, *A&A*, 49, 137
- Churazov, E., Brügger, M., Kaiser, C. R., Böhringer, H., & Forman, W. 2001, *ApJ*, 554, 261, doi: [10.1086/321357](https://doi.org/10.1086/321357)
- Churazov, E., Forman, W., Jones, C., & Böhringer, H. 2000, *A&A*, 356, 788
- Churazov, E., Ruszkowski, M., & Schekochihin, A. 2013, *MNRAS*, 436, 526, doi: [10.1093/mnras/stt1594](https://doi.org/10.1093/mnras/stt1594)
- de Koff, S., Baum, S. A., Sparks, W. B., et al. 1996, *ApJS*, 107, 621, doi: [10.1086/192376](https://doi.org/10.1086/192376)
- de Vries, W. H., O’Dea, C. P., Baum, S. A., & Barthel, P. D. 1999, *ApJ*, 526, 27, doi: [10.1086/307967](https://doi.org/10.1086/307967)
- Dopita, M. A., & Sutherland, R. S. 1995, *ApJ*, 455, 468, doi: [10.1086/176596](https://doi.org/10.1086/176596)
- . 1996, *ApJS*, 102, 161, doi: [10.1086/192255](https://doi.org/10.1086/192255)
- Dunkley, J., Komatsu, E., Nolta, M. R., et al. 2009, *ApJS*, 180, 306, doi: [10.1088/0067-0049/180/2/306](https://doi.org/10.1088/0067-0049/180/2/306)
- Ettori, S., & Balestra, I. 2009, *A&A*, 496, 343, doi: [10.1051/0004-6361:200811177](https://doi.org/10.1051/0004-6361:200811177)
- Fabian, A. C. 2012, *ARA&A*, 50, 455, doi: [10.1146/annurev-astro-081811-125521](https://doi.org/10.1146/annurev-astro-081811-125521)
- Fanaroff, B. L., & Riley, J. M. 1974, *MNRAS*, 167, 31P, doi: [10.1093/mnras/167.1.31P](https://doi.org/10.1093/mnras/167.1.31P)
- Forman, W., Churazov, E., Jones, C., et al. 2017, *ApJ*, 844, 122, doi: [10.3847/1538-4357/aa70e4](https://doi.org/10.3847/1538-4357/aa70e4)
- Fosbury, R. A. E. 1986, in *Astrophysics and Space Science Library*, Vol. 121, Structure and Evolution of Active Galactic Nuclei, ed. G. Giuricin, M. Mezzetti, M. Ramella, & F. Mardirossian, 297–306
- Fruscione, A., McDowell, J. C., Allen, G. E., et al. 2006, in *Proc. SPIE*, Vol. 6270, Society of Photo-Optical Instrumentation Engineers (SPIE) Conference Series, 62701V
- Gaspari, M., Brighenti, F., & Temi, P. 2015, *A&A*, 579, A62, doi: [10.1051/0004-6361/201526151](https://doi.org/10.1051/0004-6361/201526151)
- Gitti, M., Brighenti, F., & McNamara, B. R. 2012, *Advances in Astronomy*, 2012, 950641, doi: [10.1155/2012/950641](https://doi.org/10.1155/2012/950641)
- Gopal-Krishna, & Wiita, P. J. 2000, *A&A*, 363, 507
- Hansen, L., Jorgensen, H. E., & Norgaard-Nielsen, H. U. 1987, *A&AS*, 71, 465
- Hardcastle, M. J., Evans, D. A., & Croston, J. H. 2009, *MNRAS*, 396, 1929, doi: [10.1111/j.1365-2966.2009.14887.x](https://doi.org/10.1111/j.1365-2966.2009.14887.x)
- Hudson, D. S., Mittal, R., Reiprich, T. H., et al. 2010, *A&A*, 513, A37, doi: [10.1051/0004-6361/200912377](https://doi.org/10.1051/0004-6361/200912377)
- Intema, H. T., Jagannathan, P., Mooley, K. P., & Frail, D. A. 2017, *A&A*, 598, A78, doi: [10.1051/0004-6361/201628536](https://doi.org/10.1051/0004-6361/201628536)
- Jones, C., Forman, W., Vikhlinin, A., et al. 2002, *ApJL*, 567, L115, doi: [10.1086/340114](https://doi.org/10.1086/340114)
- Kaiser, C. R., & Best, P. N. 2007, *MNRAS*, 381, 1548, doi: [10.1111/j.1365-2966.2007.12350.x](https://doi.org/10.1111/j.1365-2966.2007.12350.x)
- Kapińska, A. D., Terentev, I., Wong, O. I., et al. 2017, *AJ*, 154, 253, doi: [10.3847/1538-3881/aa90b7](https://doi.org/10.3847/1538-3881/aa90b7)
- Kharb, P., Lister, M. L., & Cooper, N. J. 2010, *ApJ*, 710, 764, doi: [10.1088/0004-637X/710/1/764](https://doi.org/10.1088/0004-637X/710/1/764)
- Kocevski, D. D., Ebeling, H., Mullis, C. R., & Tully, R. B. 2007, *ApJ*, 662, 224, doi: [10.1086/513303](https://doi.org/10.1086/513303)
- Lovisari, L., Reiprich, T. H., & Schellenberger, G. 2015, *A&A*, 573, A118, doi: [10.1051/0004-6361/201423954](https://doi.org/10.1051/0004-6361/201423954)
- Madrid, J. P., Chiaberge, M., Floyd, D., et al. 2006, *ApJS*, 164, 307, doi: [10.1086/504480](https://doi.org/10.1086/504480)
- Main, R. A., McNamara, B. R., Nulsen, P. E. J., Russell, H. R., & Vantyghem, A. N. 2017, *MNRAS*, 464, 4360, doi: [10.1093/mnras/stw2644](https://doi.org/10.1093/mnras/stw2644)
- Markevitch, M., & Vikhlinin, A. 2007, *PhR*, 443, 1, doi: [10.1016/j.physrep.2007.01.001](https://doi.org/10.1016/j.physrep.2007.01.001)
- Markwardt, C. B. 2009, in *Astronomical Society of the Pacific Conference Series*, Vol. 411, Astronomical Data Analysis Software and Systems XVIII, ed. D. A. Bohlender, D. Durand, & P. Dowler, 251
- Massaro, F., Harris, D. E., Tremblay, G. R., et al. 2013, *ApJS*, 206, 7, doi: [10.1088/0067-0049/206/1/7](https://doi.org/10.1088/0067-0049/206/1/7)
- . 2010, *ApJ*, 714, 589, doi: [10.1088/0004-637X/714/1/589](https://doi.org/10.1088/0004-637X/714/1/589)
- Massaro, F., Tremblay, G. R., Harris, D. E., et al. 2012, *ApJS*, 203, 31, doi: [10.1088/0067-0049/203/2/31](https://doi.org/10.1088/0067-0049/203/2/31)
- Massaro, F., Harris, D. E., Liuzzo, E., et al. 2015, *ApJS*, 220, 5, doi: [10.1088/0067-0049/220/1/5](https://doi.org/10.1088/0067-0049/220/1/5)
- Massaro, F., Missaglia, V., Stuardi, C., et al. 2018, *ApJS*, 234, 7, doi: [10.3847/1538-4365/aa8e9d](https://doi.org/10.3847/1538-4365/aa8e9d)
- McNamara, B. R., Kazemzadeh, F., Rafferty, D. A., et al. 2009, *ApJ*, 698, 594, doi: [10.1088/0004-637X/698/1/594](https://doi.org/10.1088/0004-637X/698/1/594)
- McNamara, B. R., & Nulsen, P. E. J. 2007, *ARA&A*, 45, 117, doi: [10.1146/annurev.astro.45.051806.110625](https://doi.org/10.1146/annurev.astro.45.051806.110625)

- Morandi, A., Sun, M., Forman, W., & Jones, C. 2015, MNRAS, 450, 2261, doi: [10.1093/mnras/stv660](https://doi.org/10.1093/mnras/stv660)
- Osterbrock, D. E., & Ferland, G. J. 2006, *Astrophysics of gaseous nebulae and active galactic nuclei*
- Owers, M. S., Nulsen, P. E. J., Couch, W. J., & Markevitch, M. 2009, ApJ, 704, 1349, doi: [10.1088/0004-637X/704/2/1349](https://doi.org/10.1088/0004-637X/704/2/1349)
- Parma, P., Murgia, M., Morganti, R., et al. 1999, A&A, 344, 7
- Piffaretti, R., Arnaud, M., Pratt, G. W., Pointecouteau, E., & Melin, J.-B. 2011, A&A, 534, A109, doi: [10.1051/0004-6361/201015377](https://doi.org/10.1051/0004-6361/201015377)
- Randall, S. W., Nulsen, P. E. J., Jones, C., et al. 2015, ApJ, 805, 112, doi: [10.1088/0004-637X/805/2/112](https://doi.org/10.1088/0004-637X/805/2/112)
- Sarazin, C. L. 1986, *Reviews of Modern Physics*, 58, 1, doi: [10.1103/RevModPhys.58.1](https://doi.org/10.1103/RevModPhys.58.1)
- Scannapieco, E., Silk, J., & Bouwens, R. 2005, ApJL, 635, L13, doi: [10.1086/499271](https://doi.org/10.1086/499271)
- Shabala, S. S., Ash, S., Alexander, P., & Riley, J. M. 2008, MNRAS, 388, 625, doi: [10.1111/j.1365-2966.2008.13459.x](https://doi.org/10.1111/j.1365-2966.2008.13459.x)
- Spinrad, H., Marr, J., Aguilar, L., & Djorgovski, S. 1985, PASP, 97, 932, doi: [10.1086/131647](https://doi.org/10.1086/131647)
- Stuardi, C., Missaglia, V., Massaro, F., et al. 2018, ApJS, 235, 32, doi: [10.3847/1538-4365/aaafcf](https://doi.org/10.3847/1538-4365/aaafcf)
- Su, Y., Nulsen, P. E. J., Kraft, R. P., et al. 2017, ApJ, 847, 94, doi: [10.3847/1538-4357/aa8954](https://doi.org/10.3847/1538-4357/aa8954)
- Tremblay, G. R., O’Dea, C. P., Baum, S. A., et al. 2010, ApJ, 715, 172, doi: [10.1088/0004-637X/715/1/172](https://doi.org/10.1088/0004-637X/715/1/172)
- Tremblay, G. R., Chiaberge, M., Sparks, W. B., et al. 2009, ApJS, 183, 278, doi: [10.1088/0067-0049/183/2/278](https://doi.org/10.1088/0067-0049/183/2/278)
- Tremblay, G. R., O’Dea, C. P., Baum, S. A., et al. 2012, MNRAS, 424, 1026, doi: [10.1111/j.1365-2966.2012.21281.x](https://doi.org/10.1111/j.1365-2966.2012.21281.x)
- Zirbel, E. L. 1996, ApJ, 473, 713, doi: [10.1086/178184](https://doi.org/10.1086/178184)